




ORIGINAL ARTICLE

Indentation densification of fused silica assessed by raman spectroscopy and constitutive finite element analysis

Sebastian Bruns¹  | Tobias Uesbeck² | Sindy Fuhrmann³ | Mariona Tarragó Aymerich² | Lothar Wondraczek³  | Dominique de Ligny²  | Karsten Durst¹

¹Physical Metallurgy, TU Darmstadt, Darmstadt, Germany

²Institute of Glass and Ceramics, FAU, Erlangen, Germany

³Otto Schott Institute of Materials Research, University of Jena, Jena, Germany

Correspondence

Sebastian Bruns, Physical Metallurgy, TU Darmstadt, Germany.
Email: s.bruns@phm.tu-darmstadt.de

Funding information

Deutsche Forschungsgemeinschaft, Grant/Award Number: SPP 1594

Abstract

Inelastic deformation of anomalous glasses manifests in shear flow and densification of the glass network; the deformation behavior during indentation testing is linked strongly to both processes. In this paper, the indentation densification field of fused silica is investigated using depth-resolved Raman spectroscopy and finite element simulations. Through affecting the size of the indent, the normal load and the Raman laser spot size determine the spatial sampling resolution, leading to a certain degree of structural averaging. For appropriate combinations of normal load (indent size) and laser spot diameter, a maximum densification of 18.4% was found at the indent center. The indentation behavior was modeled by extended Drucker-Prager-Cap (DPC) plasticity, assuming a sigmoidal hardening behavior of fused silica with a densification saturation of 21%. This procedure significantly improved the reproduction of the experimental densification field, yielding a maximum densification of 18.2% directly below the indenter tip. The degree of densification was found to be strongly linked to the hydrostatic pressure limit below the indenter in accordance to Johnson's expanding cavity model (*J. Mech. Phys. Solids*, 18 (1970) 115). Based on the good overlap between FEA and Raman, an alternative way to extract the empirical correlation factor m , which scales structural densification to Raman spectroscopic observations, is obtained. This approach does not require the use of intensive hydrostatic compaction experiments.

KEYWORDS

densification, drucker-prager-cap plasticity, finite element analysis, fused silica, indentation, Raman Spectroscopy

1 | INTRODUCTION

Plastic deformation in oxide glasses can occur through volume-conservative shear flow or through structural densification (depending on the availability of free volume). Glasses in which the densification effect is dominant are often referred to as anomalous.^{1–3} The densification capability of

a glass reflects in its Poisson ratio ν , which in turn is linked to atomic packing density.^{4–7} Shear flow plays a major role in the deformation behavior of bulk metallic glasses (with a high Poisson ratio), whereas substantial densification occurs in classical network-forming glasses with a low Poisson ratio.

Fused silica exhibits a Poisson ratio ranging from 0.15 to 0.18. It can be densified by up to 21%^{7–10} and is often taken

This is an open access article under the terms of the Creative Commons Attribution-NonCommercial-NoDerivs License, which permits use and distribution in any medium, provided the original work is properly cited, the use is non-commercial and no modifications or adaptations are made.

© 2020 The Authors. *Journal of the American Ceramic Society* published by Wiley Periodicals, Inc. on behalf of American Ceramic Society (ACERS)

as a model for studying the densification behavior of glasses. Diamond anvil cell (DAC) experiments are typically employed for this purpose. Figure 1 shows the progress of densification with applied hydrostatic stress for fused silica according to previous studies.^{7,11,12} For describing the progress of densification, an empirical sigmoidal fit is usually used,⁷

$$\frac{\Delta\rho}{\rho_0} [\%] = \frac{\alpha}{1 + \beta \cdot \exp(-P/P_0)} - \frac{\alpha}{1 + \beta} \quad (1)$$

Here, P is the hydrostatic pressure, and α , β , and P_0 are fitting parameters. The value of α is usually small compared to the value of β and corresponds to the maximum densification (i.e. $\alpha = 21\%$ for fused silica). P_0 represents the hydrostatic pressure at the onset of densification. It was observed experimentally that irreversible densification initiates between 8 and 9 GPa under pure hydrostatic pressure.^{7,9}

Densification of glasses can also be studied in situ, for example, by combining a DAC with a Raman spectrometer. The high achievable hydrostatic pressure (about 25 GPa) allows one to study the full densification of the material.^{7,9,12,13} In this way, structural changes such as in the inter-tetrahedral Si–O–Si angle or variations in ring statistics can be directly monitored using the Raman spectrum.^{14–16} Most studies on fused silica focus on the positions of the defect lines D1 (at ambient pressure found at $\sim 470 \text{ cm}^{-1}$) and D2 ($\sim 600 \text{ cm}^{-1}$).^{15–17} However, since the D1 line merges with the main band for pressures above $p \sim 12 \text{ GPa}$, band assignments become less clear.¹⁰ In the simplest case, densification causes a band-shift to a higher energy wavenumber, reflecting the more constrained lattice with higher vibrational resonance energies.^{10,15,16,18} Deschamps et al.^{10,18} proposed a procedure to determine a Raman parameter σ , which

corresponds to the main band centroid and is determined by the inflection point of the integral of a Raman spectrum over a certain spectral range ($\sim 200\text{--}700 \text{ cm}^{-1}$). The shift of σ with applied hydrostatic pressure ($\Delta\sigma$) was found to be proportional to the degree of densification $\Delta\rho/\rho_0$,^{10,18}

$$\begin{aligned} \frac{\Delta\rho}{\rho_0} [\%] &= \frac{\sigma - \sigma_0}{\sigma_{\max} - \sigma_0} \cdot \left(\frac{\Delta\rho}{\rho_0} \right)_{\max} \\ &= \frac{\Delta\sigma}{\Delta\sigma_{\max}} \cdot \left(\frac{\Delta\rho}{\rho_0} \right)_{\max} \\ &= m \cdot \Delta\sigma \end{aligned} \quad (2)$$

In this relation σ_0 represents the initial main band centroid at ambient pressure, σ the current main band centroid at the applied pressure, and σ_{\max} the maximum band centroid of the fully densified glass (at densification $(\Delta\rho/\rho_0)_{\max}$). Then, a single factor m can correlate $\Delta\sigma$ to densification. For fused silica, a value $m = 0.2\% \text{ cm}$ was found to yield a satisfying agreement with studies relying on the analysis of individual band maxima (see Figure 1).^{7,10} Moreover, it was argued that by using Equation 2 a higher experimental reproducibility is achieved compared to using the positions of a single defect line alone.¹⁰ In addition to fused silica,^{19–21} this method was successfully applied to soda lime silicate¹⁸ and other glass systems.²²

In Raman spectroscopy lateral and depth resolution are limited by the experimental setup, i.e. the wavelength of the laser and the numerical aperture (NA) of the objective. This is a minor problem for DAC experiments, which generate a hydrostatic stress distribution and a homogeneously densified material. During indentation, a shear component can trigger the densification process²³ and once densification saturates, shear flow becomes the predominant deformation process.²⁴ Therefore, both shear and densification need to be considered as deformation mechanisms in fused silica upon indentation, resulting in complex densification gradients.^{16,18,25} Especially for small indents, such as generated at low loads (eg. in nanoindentation testing), a Raman laser probe typically averages structural information over a significant portion of the indent. In such a case the maximum band shift $\Delta\sigma$, which is present within the indent, cannot be resolved. This effect has to be taken into account when low-load indentation experiments are combined with Raman spectroscopic investigations.

Several constitutive models^{8,26–32} have been developed to describe the anomalous plastic flow behavior of fused silica. First attempts considered volume-conservative plastic shear flow using von Mises plasticity.²⁶ Later, densification-induced hardening^{8,27,28} and densification saturation, as well as changes in elastic modulus and in Poisson ratio were implemented.²⁹ Molnar et al. even found complex yield surface shape transformations which occurred upon densification.^{30,31} In direct comparison to this advanced model, the simpler approach by Kermouche et al.,²⁷ who approximated the yield surface of fused silica using an ellipse, still reproduces the load displacement

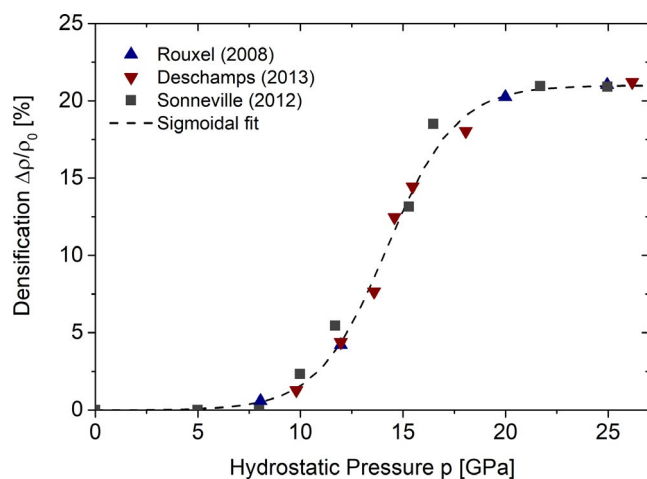


FIGURE 1 Change of densification as a function of applied hydrostatic pressure for fused silica. Data points are taken from Refs. ^{7,9,10} and the dashed line is produced from a fit to a sigmoidal function according to Equation 1 with $\alpha = 21\%$, $\beta = 4059$, $P_0 = 1.7 \text{ GPa}$ [Color figure can be viewed at wileyonlinelibrary.com]

behavior in Berkovich indentation experiments remarkably well³¹; this model was successfully transferred to soda lime glass.³³ In addition, it has been shown³⁴ that the cap section of the modified Drucker-Prager-Cap (DPC) plasticity theory is able to replicate the elliptical yield surface for fused silica.

In the present study, the densification field below indents in fused silica was analyzed using both Raman spectroscopy and FEA constitutive modeling. The obtained results are compared to DAC experiments from literature. Different indent sizes and Raman laser spot sizes were used to study the influence of structural averaging within the Raman signal. Based on experimental DAC results, the Drucker-Prager-Cap approach in FEA was extended by implementing sigmoidal densification hardening followed by densification saturation (Figure 1). The densification profiles from FEA and Raman spectroscopy are evaluated, compared, and discussed. Finally an alternative way to extract the empirical correlation factor m on the basis of FEA densification and Raman spectroscopic band shift data is suggested.

2 | EXPERIMENTAL METHODS

Commercial silica glass (Corning 7980) was employed throughout this study. Nanoindentation testing was performed using a Keysight G200 nanoindenter at room temperature under ambient pressure. Three-sided pyramidal diamond tips having centerline-to-face angles θ of 65.27° (Berkovich), 50°, and 35.26° (Cube Corner) produced by Synton-MDP were used for indentation testing. Machine compliance and tip area function were calibrated in Continuous-Stiffness-Measurement (CSM) mode according to the procedure of Oliver and Pharr.³⁵ Indentation testing was conducted in Constant-Strain-Rate (CSR) mode with an indentation strain rate of $\dot{\epsilon} = 0.2 \text{ seconds}^{-1}$. At least nine indentations were executed and the median load-displacement (LD) curve was used for comparison to FEA. The indents for subsequent Raman spectroscopic investigations were conducted in high load mode (up to 10 N) using a constant loading rate of 0.1 N/s. A Vickers indenter geometry was used to ensure comparability with densification maps available in literature.^{16,18,25,36}

Raman spectroscopy was performed on a Thermo Fisher Scientific Nicolet Almega XR Raman spectrometer coupled to an Olympus microscope. The preparation of unaltered cross sections of indents for investigation with Raman spectroscopy is rather difficult. Instead, Vickers indents with loadings ranging from 0.3 to 10 N were scanned from a top view. The spectra were collected for 532 nm laser excitation through either a 50× (NA = 0.75) or a 100× (NA = 0.9) objective with three consecutive measurements of 300 seconds for each point. A pinhole was used to achieve confocal conditions. The objectives exhibited a depth of focus (DOF) of 3.78 and 2.63 μm and a spot diameter (waist) of 0.87 and 0.72 μm , respectively, taken as the diffraction limits.³⁷

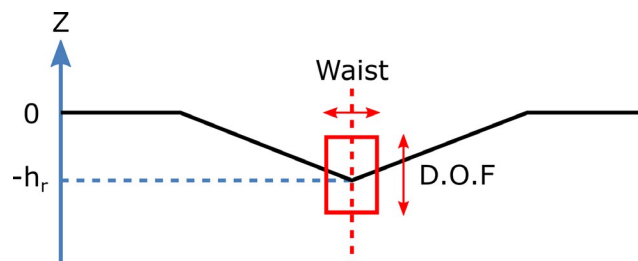


FIGURE 2 Schematic of the Z-scan. The red rectangle is a very simplified representation of the laser spot [Color figure can be viewed at wileyonlinelibrary.com]

Depth profiles (Z-scan) were recorded starting at the pristine glass surface by moving the stage with a step size of 0.5 μm until a total displacement of up to 35 μm was reached. Figure 2 shows a sketch of such a Z-Scan.

The spectra were processed according to the method described by Deschamps et al.^{10,18} in order to determine the centroid σ of the main band (region between ~ 200 and $\sim 700 \text{ cm}^{-1}$). The Z-scans were used to determine the maximum band shift observable upon indentation.

3 | COMPUTATIONAL METHODS

Finite element analysis was performed using the software package ABAQUS/Standard. The indentation process was modeled in a two dimensional (2D, $x/y-z$) axisymmetric model using the corresponding equivalent cone for the examined indenter geometries. It is worth mentioning that Vickers and Berkovich indenter exhibit the same projected contact area. Hence, both geometries share the same equivalent-conical indenter with an opening angle of 70.3°. Axisymmetry was enforced along indentation axis Z and the base was fixed with an encastre boundary condition. A total number of 3.5×10^5 full integrating axisymmetric elements (CAX4) was used to model the indentation process with a refined mesh in the vicinity of the indenter/material contact where mesh size dependency was checked. The contact between indenter and material surface was assumed to be frictionless.

All material properties were presumed to be rate insensitive, elastically isotropic, and representing room-temperature values. An elastic modulus E of 70 GPa and a Poisson ratio of 0.17 were used as input for simulation. The yield model is described in section 4.2.

4 | RESULTS AND DISCUSSION

4.1 | Indentation densification field of silica glass by Raman spectroscopy

Raman spectroscopy has become a popular tool to investigate the indentation densification behavior of normal and

anomalous glasses.^{16–18,25,36,38} However, the application of Raman spectroscopy for this purpose is by no means trivial. Especially for small indents (where the Raman laser spot size is large compared to the indent size), the structural signal of different densification states will be averaged. This effect is studied for a variety of indentation loads and different Raman excitation spot sizes in this section.

A Z-scan profiling procedure was performed at the indent center to determine the band shift as a function of the laser spot depth. Therefore, a reference Z-scan on a pristine fused silica surface was measured and σ_0 was determined and averaged to $398.4 \pm 0.4 \text{ cm}^{-1}$ over $5 \mu\text{m}$ starting at the sample surface. At the indent center the σ value exhibits an initial increase, followed by a maximum and a subsequent decrease with

decreasing Z (Figure 3A). The zero level of the Z-scan was determined optically at roughly the pristine glass surface level with a precision of $\pm 0.5 \mu\text{m}$. The Z-position of the maximum, Z_{max} (where the largest σ value was measured, $\sigma_{Z_{\text{max}}}$) corresponds approximately to the residual indentation depth h_r , identified as the color hatched regions in Figure 3A. Thus, the densification maximum, identified by $\sigma_{Z_{\text{max}}}$, is located close to the tip of the indent.^{16,27} This implies that the first focal locations at the indent center is positioned in air above the surface. Similar observations have been made on the pristine surface when the reference profile was recorded. Even $5 \mu\text{m}$ above the surface low-intensity spectra of fused silica were detectable when using a defocused laser beam (Figure S1F). This implies that the defocused beam interacts with the material already at focal distances above the actual sample surface.

In a first approximation, the focus region is taken as a rectangle (Figure 2). At h_r only half of the DOF has penetrated into the glass. Full interaction will take place at focal positions below the surface only. For a more exact analysis, the change in refractive index between ambient air and the glass need to be taken into account.³⁹ As for the present case, we have an indent shape with tilted walls partially reflecting the laser beam and further enhancing the complexity of the situation. Yet, it is clear that the largest σ value, $\sigma_{Z_{\text{max}}}$, is related to the most densified region within the indent.

The problem of structural averaging within the Raman laser spot becomes obvious when comparing Z-scans for different indentation loads. The value of $\sigma_{Z_{\text{max}}}$ increases with increasing indent size (Figure 3A). This indicates that structural averaging over a densification gradient is more pronounced in small indents where the laser spot size is big compared to the indent size. The Raman spectra at Z_{max} , which correspond to $\sigma_{Z_{\text{max}}}$, indicated by a star in Figure 3A, are shown in Figure 3B. With increasing indentation load the shift of the main band toward larger wavenumbers becomes more pronounced (with respect to the black reference spectrum). The spectra for 5 and 10 N are almost identical (orange vs blue spectrum). A similar structural averaging effect can be observed when the laser spot size is increased by switching objectives from 100 \times to 50 \times (Figure S2F).

The densification was determined from the Raman main band shift using Equation 2 with a correlation value $m = 0.2\%$ cm with $\Delta\sigma = \sigma_{Z_{\text{max}}} - \sigma_0$. This densification value is henceforth referred to as “Raman evaluated densification”. A spherical equivalent laser focus spot with a radius r (half the average of DOF and laser waist) was assumed in this analysis. This laser spot size r was normalized to the size of the residual indentation depth h_r .³⁵ In reality, the laser spot geometry is more complex and further refraction effects occur. The obtained densification as a function of the normalized parameter r/h_r is plotted for a variety of indentation loads and two different objectives in Figure 4 and summarized in Table 1.

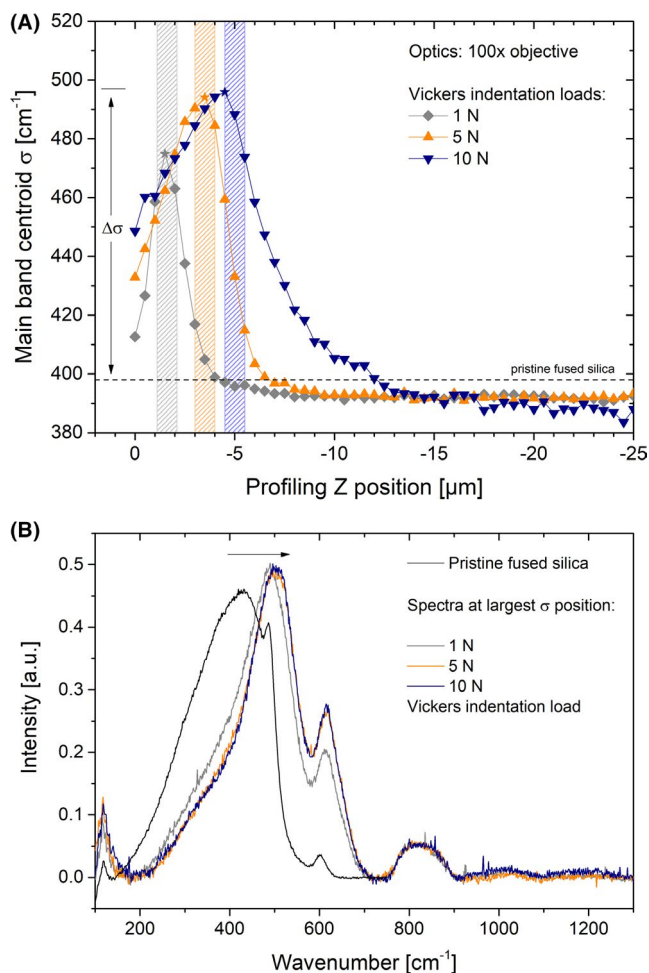


FIGURE 3 (A) Raman Z-scan of σ at the center of Vickers indentations in fused silica for a variety of indentation loads. A larger $\Delta\sigma$ is found in larger indents. The hatched regions represent the expected positions of the residual indentation depth h_r taking the error on the determination of the surface level into account. The Raman spectra (baseline corrected and normalized) at $\sigma_{Z_{\text{max}}}$ position (indicated by a star) are shown in (B). A reference spectrum of the pristine glass surface is shown in black. The spectra for loading at 5 or 10 N are practically identical [Color figure can be viewed at wileyonlinelibrary.com]

With decreasing r/h_r the extent of structural averaging decreases, consequently larger Raman evaluated densification values are obtained for larger indent sizes. The normalization procedure aimed to achieve comparability between the 50 \times objective and 100 \times objective data. A small offset remains, which is likely based on simplifications made regarding the laser spot geometry. For r/h_r values smaller than 0.3 the obtained Raman evaluated densification converged to a single value indicating that a homogeneously densified region is probed. Those findings are supported by the Raman spectra, where no further band shift can be observed between 5 and 10 N of normal load (Figure 3B).

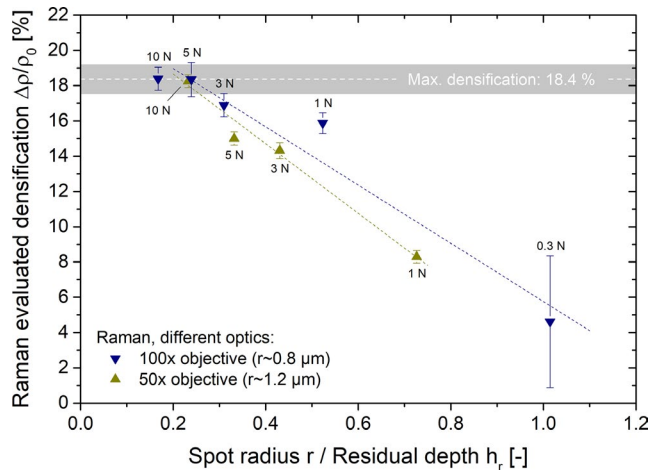


FIGURE 4 The Raman evaluated densification at the indent center as a function of the laser spot size r normalized by the residual indentation depth h_r . The residual indentation depth h_r was varied by applying different indentation loads, hence the laser spot in Raman spectroscopy averages over different densification gradients. Additionally, the laser spot radius was varied by using different objectives. The dotted lines represent the corresponding linear fits. The maximum Raman evaluated densification is plotted as dashed white line with the corresponding standard deviation as light grey background [Color figure can be viewed at wileyonlinelibrary.com]

Similar densification values were found at the center of the 10 N indent even for different objectives (Figure 4). Results within this range ($r/h_r < 0.3$) were averaged to a maximum Raman evaluated densification value of $18.4\% \pm 0.8\%$ (dotted white line with light grey border in Figure 4). This evaluation corresponds well to values reported for macroscopic Vickers indents in literature^{16,27,40} and indicate that a densification of 21% as found in DAC^{7–10} is not reached by (Vickers) indentation after unloading.

High indentation loads are required to develop a homogeneously densified region large enough to be resolved by the Raman microscope setup. Figure 5 shows that indents satisfying $r/h_r < 0.3$ are heavily affected by cracking. For smaller indentation loads, it is possible to find occasional indents without cracking (Figure 5A). Indents produced at loads below 3 N are mostly affected by edge cracks only, a crack type known to penetrate the material only to a relatively low depth.⁴¹ The present dataset indicates that cracking does not affect the determination of σ_{Zmax} . Yet, cracking can introduce local shape modifications and thereby affect the expected laser spot position and the shape of the σ depth profile. Moreover, energy release upon cracking may affect the observed degree of densification. Indentation under inert atmosphere and using advanced preparation techniques might shift the onset of cracking toward higher loads^{42–44} and could therefore improve laser positioning. For fused silica, 3 N appears to be a good compromise between averaging of structural information within the laser spot (the max. Raman evaluated densification is underestimated by less than 10%) and incipient cracking.

4.2 | Drucker-Prager-Cap plasticity with sigmoidal densification behavior

The anomalous flow behavior of fused silica is implemented into FEA following the approach by Bruns et al.³⁴ It could be

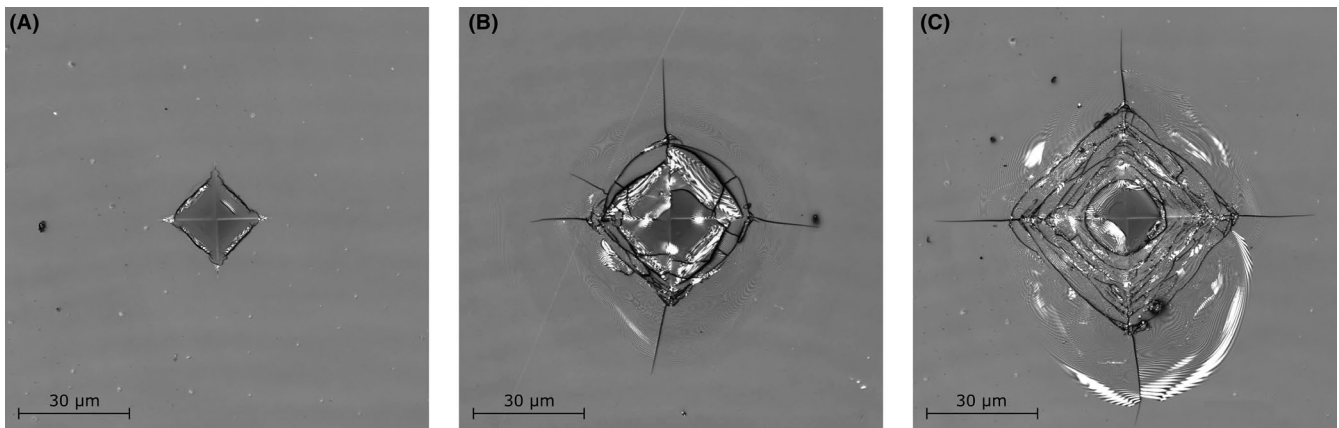


FIGURE 5 Vickers indentation crack pattern in Corning 7980 fused silica loaded with (A) 3 N, (B) 5 N, and (C) 10 N. Indents loaded with less than 3 N exhibit mostly a similar crack pattern as shown in A). Edge cracks are to some extent already present at 300 mN

TABLE 1 A summary of the σ data for the 100 \times objective Raman test series on Vickers indentations

Indentation load	300 mN	1 N	3 N	5 N	10 N
Residual depth h_r	0.85 μm	1.6 μm	2.7 μm	3.5 μm	5 μm
$\sigma_{Z\text{max}}$	$421.5 \pm 18.7 \text{ cm}^{-1}$	$477.8 \pm 2.9 \text{ cm}^{-1}$	$482.9 \pm 3.2 \text{ cm}^{-1}$	$490.2 \pm 4.8 \text{ cm}^{-1}$	$490.4 \pm 3.2 \text{ cm}^{-1}$
$\Delta\sigma$	$23.1 \pm 18.7 \text{ cm}^{-1}$	$79.4 \pm 2.9 \text{ cm}^{-1}$	$84.5 \pm 3.3 \text{ cm}^{-1}$	$91.7 \pm 4.8 \text{ cm}^{-1}$	$92.0 \pm 3.3 \text{ cm}^{-1}$
Raman evaluated densification	$4.6 \pm 3.7 \%$	$15.9 \pm 0.6 \%$	$16.9 \pm 0.7 \%$	$18.4 \pm 1.0 \%$	$18.4 \pm 0.7 \%$

shown, that the cap section of modified Drucker-Prager-Cap plasticity is suitable to depict the elliptically shaped yield surface of fused silica with a two-parameter model. For this purpose the DPC model was modified in a way that only the cap surface remains in the positive sector of the meridional (p - q) plane (Figure 6B). This is realized by assuming an initial-volumetric-inelastic strain $p_a = 0$, shifting both the Drucker-Prager failure surface and transition failure surface into the tensile region. The pressure dependency of the Drucker-Prager failure surface was eliminated by minimizing the friction angle to 10^{-4} : doing so a von Mises like failure behavior is achieved. The shape of the cap is controlled by parameter R , the cap eccentricity, which forces the yield surface to be elliptical. It corresponds to the ratio of the hydrostatic yield strength p_b to the yield strength under pure shear d . Further details on this constitutive description can be found elsewhere.^{34,45,46}

The input for the hydrostatic yield strength p_b is based on diamond anvil cell densification data from literature.^{7,9,10} Previous computational studies^{27,34} used a simplified linear approximation of the sigmoidal densification hardening behavior where yielding was assumed to initiate at 11.5 GPa followed by linear isotropic densification with a hardening slope of 100 GPa. Since this approach considers no saturation to occur, densification could theoretically continue until infinity. The present study aims to include densification saturation by a less simplified implementation of the densification hardening behavior. The fused silica hardening data from literature (Figure 1) is fitted according to Rouxel⁷ using Equation 1. Values of 21%, 4059 and 1.7 GPa were determined for α , β and P_0 respectively (Table 2). A stepwise linear approximation was used to implement the sigmoidal densification behavior as input for yielding under pure hydrostatic compression into ABAQUS. A plastic strain ϵ_{pl} exceeding 1% was assumed as the onset point for densification p_b . This corresponds to a hydrostatic pressure of 8 GPa, which corresponds well to the onset of densification reported in literature.^{7,9,18,27}

The input for the yield strength under pure shear d is determined following the approach proposed by Kermouche et al.²⁷ using an inverse analysis of nanoindentation load displacement (LD) curves. Experimental LD curves were recorded for three different indenter geometries (ie Cube Corner, 50 $^\circ$ and Berkovich) and compared to the FEA LD output for different values of d . The best fit was found for a d value of 7.5 GPa

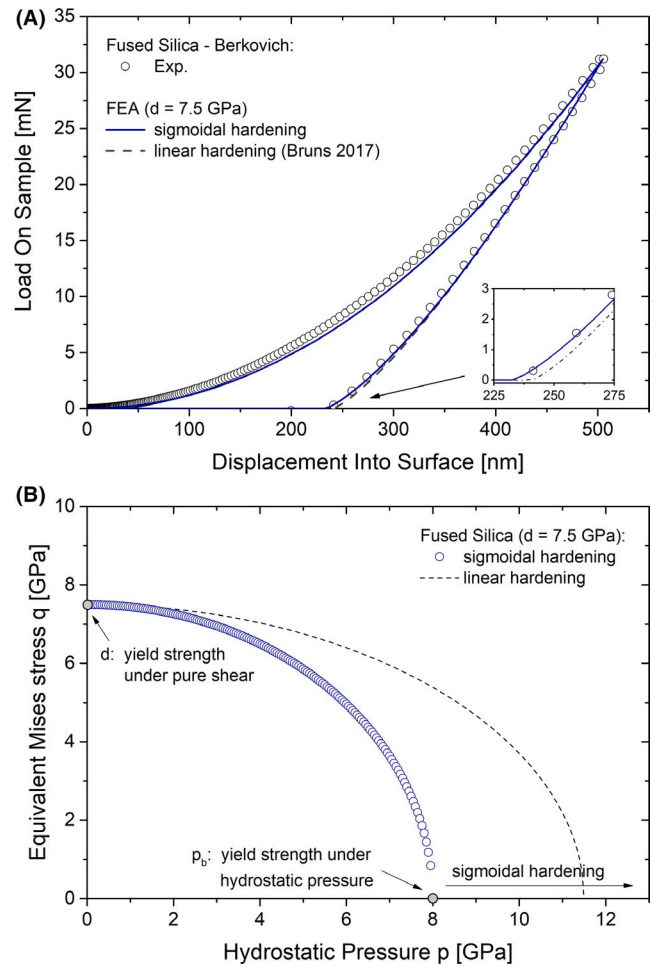


FIGURE 6 A, Nanoindentation load displacement curves (open circles) are fitted to calibrate d , the yield strength under pure shear, exemplarily shown for Berkovich indented fused silica. B, The final Drucker-Prager-Cap including sigmoidal densification behavior as input for yielding under hydrostatic compression is sketched as open blue symbols. The onset of densification p_b shifts toward higher p as indicated by “sigmoidal hardening” labeled arrow. The calibration of a previous study³⁴ (with linear densification behavior) is sketched as dotted line for comparison [Color figure can be viewed at wileyonlinelibrary.com]

(Figure 6A), comparable to d values found in literature.^{23,34,47} With the given pair of yield strengths (p_b and d), the cap eccentricity R can be calculated by $p_b/d \approx 1.067$. The resulting yield surface for fused silica is sketched in Figure 6B. All material parameters used in the present study are summarized in Table 2.

A 2D axisymmetric model with a 70.3° Berkovich/Vickers equivalent conical indenter is used to study the influence of the densification hardening behavior on the indentation response. The implementation of sigmoidal instead of linear densification hardening has a small influence on the nanoindentation load displacement response (Figure 6A). This agrees well with Molnar's³¹ observation that small changes in the densification behavior exhibit only a negligible effect on the macroscopic LD response. The densification field beneath the residual impression (Figure 7) can be visualized using the volumetric inelastic strain, which is given by the parameter PEQC4 in ABAQUS. The linear densification DPC model does not consider densification saturation. Thus, densification values in the range of up to 100%-170% are reached in the zone immediately beneath the indenter tip at the indent center (Figure 7, left side). Consequently, densification is strongly overestimated. The sigmoidal hardening DPC model in turn delivers a maximum densification value of 18.2% at the indent center (element face output). This value is in good agreement with both the maximum Raman evaluated densification value of 18.4% (Figure 4) and the densification profiles present in literature.^{16,27,28,33,40} Furthermore, the input densification saturation value of 21% is not reached in the simulation. With sigmoidal densification hardening the densification field penetrates deeper into the material and spreads larger

toward the surface while maintaining the half penny contour shape longer with ongoing densification. This effect can be attributed to the earlier onset of densification p_b (8 vs 11.5 GPa) considered in the sigmoidal hardening law.

The sigmoidal densification hardening implementation gives a far better description of the experimentally observed anomalous deformation behavior of fused silica and will be used in all further investigations.

4.3 | Influences of FEA tip geometry on the densification maximum in indentation testing

The FEA indentation simulation (Figure 7, right side) did not achieve the densification saturation value of fused silica (21%) from literature⁷⁻¹⁰ when using the equivalent cone of Berkovich/Vickers geometry. Stress trajectories in p - q plane provide additional insight into the plastic flow and densification behavior during deformation.^{23,31} Figure 8A shows exemplarily a stress trajectory for a single element at the indent center upon loading. The initial deformation is purely elastic until the trajectory enters the yield cap at a hydrostatic pressure of about 1.5 to 2 GPa. Yielding is followed by densification, showing that the shear stress component (about 7.35 GPa) causes densification to initiate at a lower hydrostatic pressure component compared to DAC.

TABLE 2 Drucker-Prager Cap calibration with sigmoidal densification hardening data for fused silica

Glass	Poisson's ratio ν	E [GPa]	Drucker-Prager-Cap		Sigmoidal hardening ^a		
			d [GPa]	p_b [GPa]	α [%]	β	P_0 [GPa]
Fused Silica	0.17	70	7.5	8	21.0	4059	1.7

^aDensification data taken from the studies by Rouxel, Deschamps and Sonnevile,^{7,9,10} see also Figure 1.

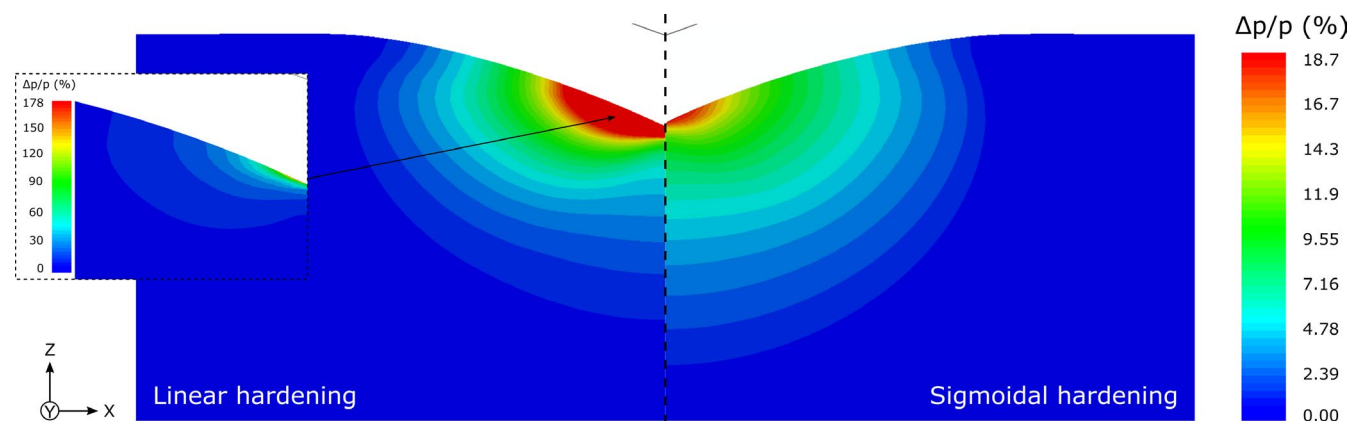


FIGURE 7 A PEQC4 contour plot export from ABAQUS showing the FEA densification profile beneath the indent of a Vickers/Berkovich equivalent cone with an opening angle of 70.3° in fused silica after unloading (side view). Drucker-Prager-Cap plasticity with linear (left) and sigmoidal (right) densification behavior is compared. A similar view was used for both exports in order to visualize differences in densification field expansion. The scale was chosen to represent the max. nodal output of the sigmoidal approach. This has the consequence that all larger densification values present in the linear approach are not visible. Therefore, the dashed box provides a scale oriented on the max. nodal output of the linear hardening model [Color figure can be viewed at wileyonlinelibrary.com]

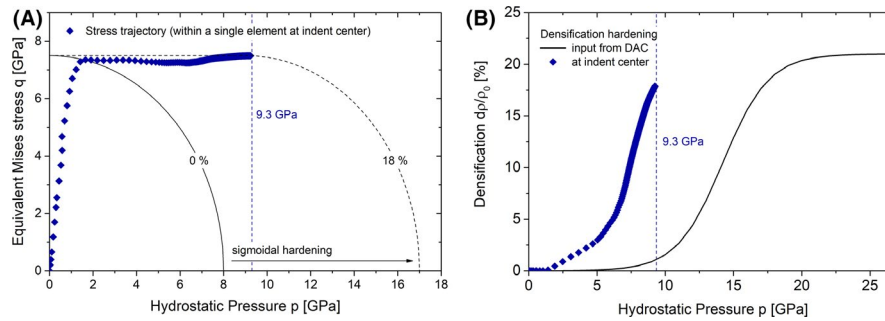


FIGURE 8 A, Stress trajectory of a single element at indent center while loading with the eq. cone of Berkovich/ Vickers geometry. B, The densification state within the single element at indent center as a function of the hydrostatic pressure. The densification input from DAC^{7,9,10} is sketched for comparison [Color figure can be viewed at wileyonlinelibrary.com]

With ongoing (sigmoidal) densification the stress trajectory propagates almost parallel to the p -axis. The shear component rises, roughly at a point where the slope in the sigmoidal densification hardening curve is steepest, and the densification limit of about 18% determined for Berkovich/Vickers geometry is approached at a hydrostatic pressure of about 9.3 GPa. From this point on, the deformation consists mainly of growth of the plastic zone without a further increase of the densification maximum value. This behavior is similar to Johnson's expanding cavity model, which describes the self-similar extension of the plastic zone below the indenter for elastic-plastic materials.⁴⁸ The densification as a function of the hydrostatic stress component is shown in Figure 8B. Starting from a hydrostatic stress of about 2 GPa an increase in density becomes noticeable, which corresponds to those data points in Figure 8A which have passed the yield surface. Densification proceeds along the stress trajectory in a sigmoidal manner until a saturation in densification is achieved at about 18%. Compared to the pure hydrostatic DAC input, the shear component in Berkovich/ Vickers indentation lowers the onset of densification by about 6 GPa.

The data presented in Figure 8 shows the loading history of the stress states in a single element at indent center. The stress states of all elements below the indenter at maximum penetration depth can provide further useful insight into the plastic deformation.^{23,31} This corresponds to the loading situation in Figure 7 (right side). The stress state of all elements in the vicinity of the contact is therefore plotted in Figure 9A. It can be seen that the onset yielding varies with the position beneath the indenter. Areas which appeared blue in Figure 7 remained fully elastic, hence corresponding data points are located within the yield ellipse in Figure 9A. Elements which are located close to the contact situation exhibit a larger shear component than elements located deeper in the material. They require a larger hydrostatic component to initiate plasticity. The densification maximum in the range of 18% is, however, not exceeded in any of the elements.

Sharper indenter geometries are known to displace more volume and to introduce higher stresses at a given

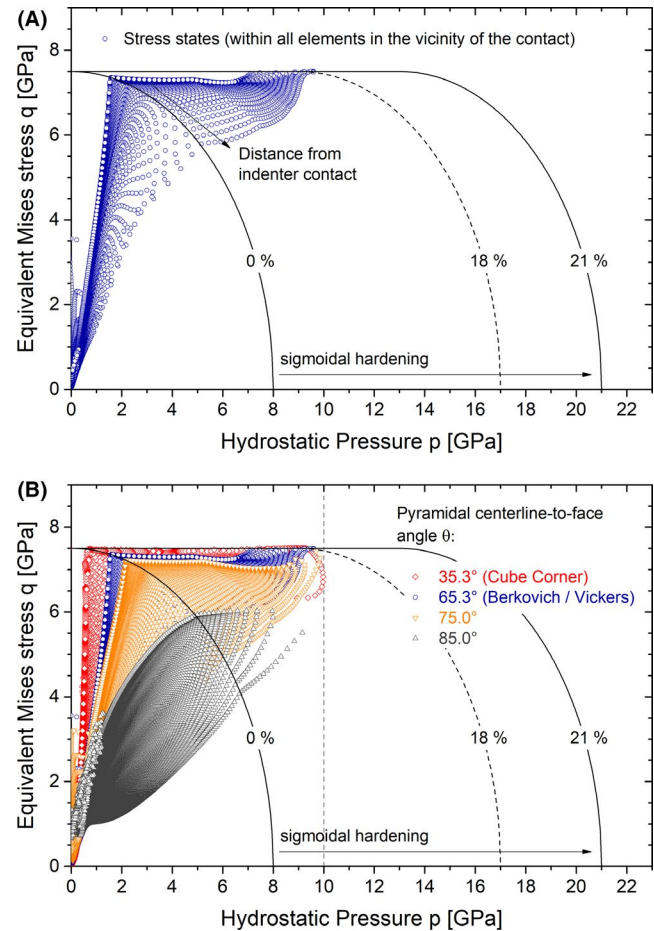


FIGURE 9 The stress states within all elements in the vicinity of the contact situation exported at maximum indenter penetration for A, Berkovich/ Vickers indenter geometry and B, a variation of the indenter centerline-to-face angle [Color figure can be viewed at wileyonlinelibrary.com]

load.⁴⁹ It is unclear, however, how the changed stress field affects the densification field beneath the impression. For this purpose, simulations of sharper ($\theta = 35.3^\circ$, cube corner) and blunter ($\theta = 75^\circ$ and $\theta = 85^\circ$) pyramidal indenter geometries with respect to the Berkovich/ Vickers geometry were performed as well. In all cases the corresponding

2D axisymmetric equivalent cone was used for simulation. The stress state distribution at peak load (Figure 9B) indicates that a decreasing indenter opening angle introduces a larger shear component. Consequently, the yield ellipse is surpassed at a smaller pressure and densification is initiated earlier for cube corner geometry (red). The maximum indentation densification interestingly does not exceed 18% either. The plastic zone expansion (sketched grey in Figure 10) covers the whole contact zone in case of cube corner geometry. The plastic zone approaches the free surface and is therefore less confined. As a result, slight pile-up formation can be observed and the position of maximum densification shifts toward the surface. For blunter indenters the plastic zone size decreases with increasing indenter opening angle. It covers a smaller part of the contact area with increasing elasticity. Therefore, higher pressures are required to introduce densification. As a result, a slightly smaller indentation densification maximum of 17.3% is observed for $\theta = 75^\circ$. This effect is even larger if blunter indenters are used, eg for $\theta = 85^\circ$ a densification value of 5% is not exceeded.

Changing from one indenter geometry to another does not necessarily result in higher densification values. The simulations indicate that the extent of densification is strongly linked to the hydrostatic pressure below the indenter, which does not exceed $P = 10$ GPa for all examined indenter geometries (Figure 9B: light grey sketched vertical line). Interestingly, this hydrostatic pressure corresponds remarkably well to fused silica's indentation hardness of about 9.6 GPa.⁵⁰ According to Hill⁵¹ and Johnson⁴⁸ the hydrostatic pressure saturates in a central region (inside the plastic zone) below the indenter. In Johnson's expanding cavity model the pressure acting within this so-called hydrostatic core corresponds approximately to the mean indentation contact pressure, ie the indentation hardness H , which is defined as the applied load per projected contact area of the indentation.^{48,52,53} If $p = H$ is reached, the hydrostatic core expands, causing thereby the extension of the plastic zone. The hydrostatic stress is thus limited, which thereby also limits the amount of densification below the indenter. Materials which exhibit a higher hardness should also sustain larger hydrostatic stresses and exhibit larger densification values. This behavior is confirmed via FEA simulations where the hardness of the material is altered by changing the input for the yield strength under pure shear in Figure SF 3. Johnson's expanding cavity model has also been applied to pressure sensitive⁵⁴ and strain hardening materials.⁵³ Due to the self-similarity of the indenter this behavior is independent of the indenter size.⁵³

For indenter geometries which are mainly used in experiments, ie θ ranging from 75° to 35° , this results in small variations of the maximum densification value, as the onset of densification differs by about 1 GPa only (Figure 8B).

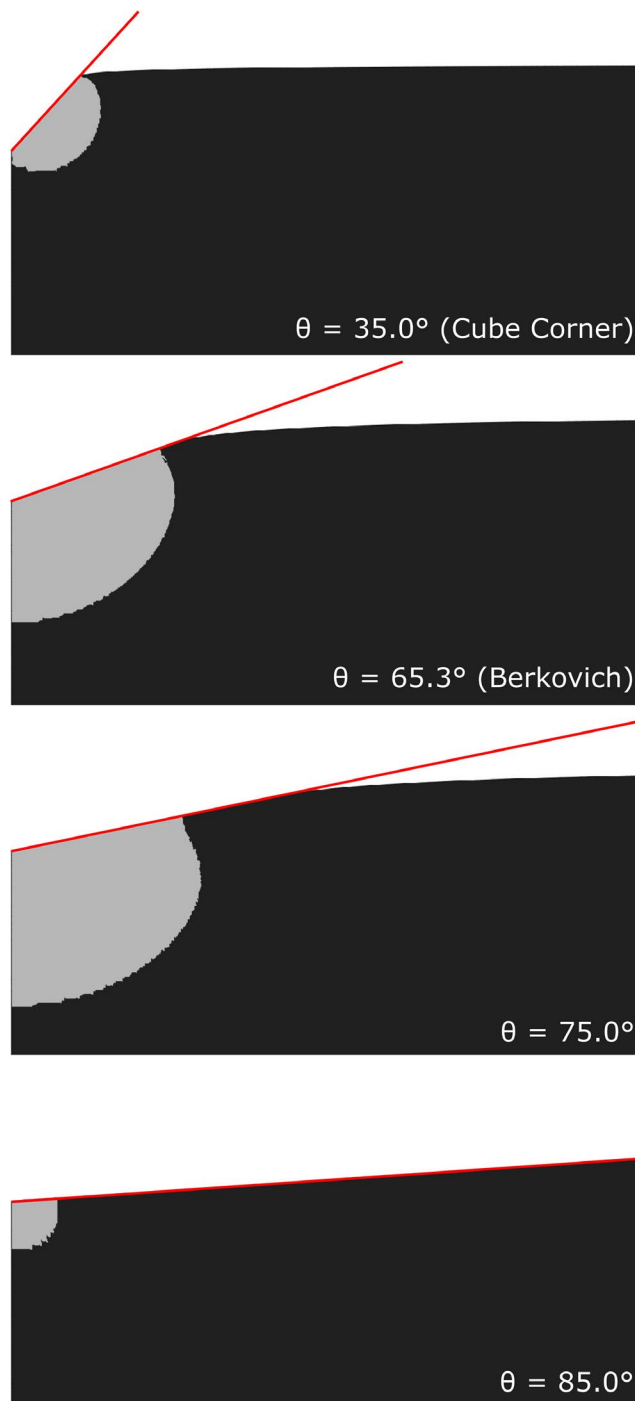


FIGURE 10 Plastic zone spread for eq. cones of various three sided pyramidal indenter geometries. The corresponding centerline-to-face angles θ are listed in the figure. The indenter is sketched in red [Color figure can be viewed at wileyonlinelibrary.com]

The plastic zone spread suggests that Berkovich/Vickers or the $\theta = 75^\circ$ geometry are nicely suited to investigate indentation densification experimentally using Raman spectroscopy. Their plastic zone does not reach the surface and is aligned more horizontally as compared to cube corner geometry. This facilitates improved lateral resolution for Raman spectroscopic investigations. The plastic zone size and with

it the densification field decrease for blunter tip geometries. Consequently, Raman spectroscopy would reach the resolution limit earlier.

4.4 | Relating FEA densification to Raman spectroscopy Z-profiling

The results presented in the previous sections have shown that FEA is capable to reproduce the indentation densification maximum determined via Raman spectroscopy with reasonable accuracy. The densification estimate from FEA exhibits both a similar dependency on the investigated volume as observed with Raman spectroscopy (not shown here) and a similar densification-depth profile (Figure 11). A normalization of the densification-depth profile to the indent size (h_r) allows comparison between different indentation loads and FEA. The Z positions of the depth profiles from Raman spectroscopy (Figure 3) were corrected with h_r in order to set the surface level to zero. The FEA profile affirms this assumption as it can only depict the densification gradient within the material. This section agrees reasonably with the Raman densification profile from Z_{\max} position onwards into the material. For larger depths, however, deviations between Raman and FEA can be noticed in Figure 11. Those deviations might either be attributed to simplifications in the FEA constitutive model or the complicated laser spot geometries and refractive effects in Raman spectroscopy (i.e. changes in the index of refraction with densification⁵⁵) which are not taken into account in this analysis.

The good correlation among the densification profiles between FEA and Raman spectroscopy at the indent center

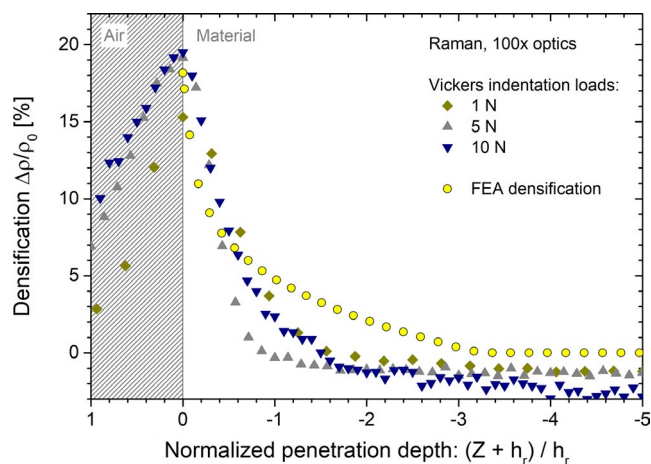


FIGURE 11 Densification-depth profiles normalized by the residual indentation depth h_r . Densification is estimated from the σ -profiles presented in Figure 3 using Equation 2. The Z position is corrected by the residual indentation depth h_r . The FEA densification estimate is based on face element output [Color figure can be viewed at wileyonlinelibrary.com]

suggests the use of simulations for Raman density calibration. The correlation factor m (Equation 2) is usually determined from Raman peak shifts measured on bulk densified samples from high-pressure experiments (eg DAC, Multi-Anvil press, etc). Density is measured with conventional methods, such as Archimedes' principle, and related to the Raman shift $\Delta\sigma$ using a linear fit (Figure 12). Using literature, this method provides a correlation constant m of 0.2% cm for fused silica.¹⁰

As already noted, the m factor from DAC experiments is useful for quantifying indentation-induced densification from band shifts in Raman spectroscopy. However, data on m are scarce and presently not available beyond fused silica and soda lime silicate glass.^{10,19,25} The present results have shown that FEA is able to provide the densification state at the indent center, hence, it can be used for densification scaling. Associating the obtained maximum of densification to the observed Raman band shift $\Delta\sigma$ at the center of 3 to 10 N indents produces three new data points (blue open hexagons) in Figure 12 (through the intersection of maximum Raman band shift with maximum densification data from simulation). The blue error bars represent the standard deviation and the light grey hatched area indicates data scatter. Then, using Equation 2 and the FEA densification value, m is estimated at $0.198 \pm 0.015\%$ cm for 5 and 10 N indentation loads. For 3 N, a different value of $0.216 \pm 0.015\%$ cm is obtained. All three indentation loads are located within the scatter field of Deschamps data (black squares) based on DAC experiments,¹⁰ showing in fact very good agreement between both methods. Thus, the procedure enables determination of the empirical m parameter without using extensive high-pressure experimentation such as DAC studies. Previous results have

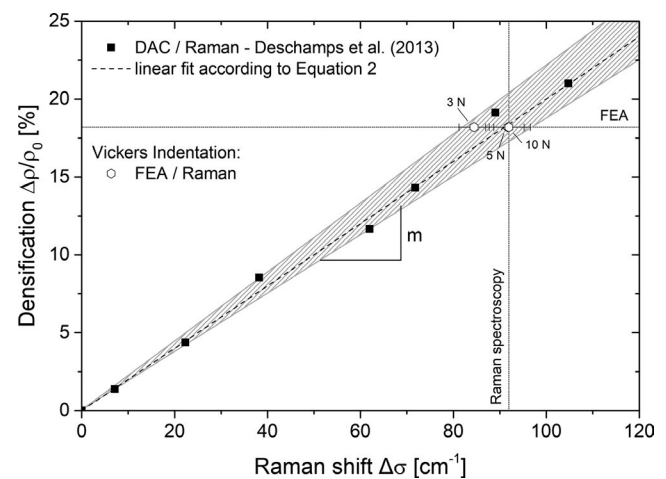


FIGURE 12 DAC densification data of fused silica (black symbols) according to Deschamps et al.¹⁰ with linear fit as black dotted line. Correlating the Raman shift in Vickers indentation center to the densification value delivered by FEA (open blue symbols) matches the DAC data surprisingly well. The standard deviation from $\Delta\sigma$ in indentation center is sketched as hatched area

shown that indentation does not reach densification saturation, so a direct correlation of $\Delta\sigma$ at the indent center to the model-predicted densification saturation value⁷ is not possible. The model prediction, however, can be used for FEA to construct the yield surface of a given glass (Figure 6). The indentation simulation can then provide the indentation densification state which belongs to the $\Delta\sigma$ determined by Raman spectroscopy. Its accuracy, however, is determined by the careful analysis of the spatial resolution of the Raman set-up.

5 | CONCLUSIONS

The investigation of densification-induced Raman band shifts requires deeper knowledge on the spatial resolution of the experimental set-up. This includes consideration of the laser focal position and spot size relative to the indent size and shape. Z-scans at the indent center are useful for examining the maximum degree of densification. For Vickers indentation on fused silica, as a practical guide, the Raman laser spot radius r should not exceed 0.3 times the residual indentation depth h_r , so as to not underestimate the maximum densification by more than 10%. We observed a maximum densification value of 18.4% for indentations loads exceeding 5 N. The loading range used in conventional nanoindentation testing (<1 N) produces indent sizes which are typically too small to resolve the given indentation densification maximum when conventional Raman microscopes are used.

The implementation of sigmoidal densification hardening for hydrostatic compaction is an effective approach in FEA to improve the Drucker-Prager-Cap constitutive description of fused silica. Even though the nanoindentation load displacement behavior is affected only slightly, the consideration of densification saturation leads to a significantly improved reproduction of the densification profile beneath (Vickers) indents. A densification value of 18.2% is determined at the indent center, a value matching the Raman evaluated densification and data presented in literature.^{16,28,33,40} The amount of densification is strongly linked to the hydrostatic pressure component below the indenter. For fused silica a p_{\max} in the range of 10 GPa was observed, which is close to the indentation hardness H of the material. This observation agrees well to expanding cavity models,^{48,53,54} where the pressure component within the hydrostatic core is limited. Further penetration expands those zones, but the hydrostatic pressure and thus the densification is limited. The homogeneously densified region found in indents satisfying $r/h_r < 0.3$ can be attributed to this behavior. The indenter geometry affects the indentation densification maximum only slightly. The plastic zone shape of various indenter geometries indicate that the Berkovich or Vickers indenter geometry are well-suited to study densification by Raman spectroscopy. Blunter indenter tips exhibit a smaller plastic zone size while for sharper indenters the plastic

zone is less confined and more vertically aligned, which are both disadvantages for Raman spectroscopic investigations.

The close agreement between Raman spectroscopy and FEA suggests that the FEA densification field can be used to estimate the empirical density correlation factor m for scaling the Raman shift to structural densification.

ACKNOWLEDGMENTS

Funding by the German Science Foundation (DFG) in priority program “SPP 1594 - Topological Engineering of Ultrastrong Glasses” is gratefully acknowledged. The authors thank Courtney Calahoo and George M. Pharr for helpful discussions.

ORCID

Sebastian Bruns  <https://orcid.org/0000-0003-1689-4750>
Lothar Wondraczek  <https://orcid.org/0000-0002-0747-3076>
Dominique de Ligny  <https://orcid.org/0000-0001-9621-4609>

REFERENCES

- Peter KW. Densification and flow phenomena of glass in indentation experiments. *J Non-Cryst Solids*. 1970;5(2):103–15.
- Ernsberger FM. Role of densification in deformation of glasses under point loading. *J Am Ceram Soc*. 1968;51(10):545–7.
- Arora A, Marshall DB, Lawn BR, Swain MV. Indentation deformation-fracture of normal and anomalous glasses. *J Non-Cryst Solids*. 1979;31(3):415–28.
- Makishima A, Mackenzie JD. Calculation of bulk modulus, shear modulus and Poisson's ratio of glass. *J Non-Cryst Solids*. 1975;17(2):147–57.
- Yoshida S, Sangleboeuf J-C, Rouxel T. Quantitative evaluation of indentation-induced densification in glass. *J Mater Res*. 2005;20(12):3404–12.
- Rouxel T. Elastic properties and short-to medium-range order in glasses. *J Am Ceram Soc*. 2007;90(10):3019–39.
- Rouxel T, Ji H, Hammouda T, Moréac A. Poisson's ratio and the densification of glass under high pressure. *Phys Rev Lett*. 2008;100(22):225501.
- Lambropoulos JC, Xu S, Fang T. Constitutive law for the densification of fused silica, with applications in polishing and microgrinding. *J Am Ceram Soc*. 1996;79(6):1441–52.
- Sonneville C, Mermet A, Champagnon B, Martinet C, Margueritat J, de Ligny D, et al. Progressive transformations of silica glass upon densification. *J Chem Phys*. 2012;137(12):124505.
- Deschamps T, Kassir-Bodon A, Sonneville C, Margueritat J, Martinet C, de Ligny D, et al. Permanent densification of compressed silica glass: a Raman-density calibration curve. *J Phys Condens Matter*. 2013;25(2):025402.
- Tse JS, Klug DD, Le Page Y. High-pressure densification of amorphous silica. *Phys Rev B*. 1992;46(10):5933–8.
- Vandembroucq D, Deschamps T, Coussa C, Perriot A, Barthel E, Champagnon B, et al. Density hardening plasticity and mechanical ageing of silica glass under pressure: a Raman spectroscopic study. *J Phys: Condens Matter*. 2008;20(48):485221.
- Deschamps T, Margueritat J, Martinet C, Mermet A, Champagnon B. Elastic moduli of permanently densified silica glasses. *Sci Rep*. 2014;4:7193.

14. Galeener FL. Planar rings in glasses. *Solid State Commun.* 1982;44(7):1037–40.
15. Sugiura H, Ikeda R, Kondo K, Yamadaya T. Densified silica glass after shock compression. *J Appl Phys.* 1997;81(4):1651–5.
16. Perriot A, Vandembroucq D, Barthel E, Martinez V, Grosvalet L, Martinet CH, et al. Raman microspectroscopic characterization of amorphous silica plastic behavior. *J Am Ceram Soc.* 2006;89(2):596–601.
17. Malchow P, Johanns KE, Möncke D, Korte-Kerzel S, Wondraczek L, Durst K. Composition and cooling-rate dependence of plastic deformation, densification, and cracking in sodium borosilicate glasses during pyramidal indentation. *J Non-Cryst Solids.* 2015;419:97–109.
18. Deschamps T, Martinet C, Bruneel JL, Champagnon B. Soda-lime silicate glass under hydrostatic pressure and indentation: a micro-Raman study. *J Phys Condens Matter.* 2011;23(3):035402.
19. Cornet A, Martinez V, Ligny DD, Champagnon B, Martinet C. Relaxation processes of densified silica glass. *J Chem Phys.* 2017;146(9):094504.
20. Romeis S, Paul J, Herre P, de Ligny D, Schmidt J, Peukert W. Local densification of a single micron sized silica sphere by uniaxial compression. *Scr Mater.* 2015;108:84–7.
21. Guerette M, Poltorak A, Fei Y, Strobel TA. Permanent densification of silica glass for pressure calibration between 9 and 20 GPa at ambient temperature. *High Pressure Res.* 2019;39(1):117–30.
22. Kato Y, Yamazaki H, Yoshida S, Matsuoka J, Kanzaki M. Measurements of density distribution around Vickers indentation on commercial aluminoborosilicate and soda-lime silicate glasses by using micro Raman spectroscopy. *J Non-Cryst Solids.* 2012;358(24):3473–80.
23. Lacroix R, Kermouche G, Teisseire J, Barthel E. Plastic deformation and residual stresses in amorphous silica pillars under uniaxial loading. *Acta Mater.* 2012;60(15):5555–66.
24. Rouxel T, Ji H, Guin JP, Augereau F, Rufflé B. Indentation deformation mechanism in glass: densification versus shear flow. *J Appl Phys.* 2010;107(9):094903.
25. Kassir-Bodon A, Deschamps T, Martinet C, Champagnon B, Teisseire J, Kermouche G. Raman mapping of the indentation-induced densification of a soda-lime-silicate glass. *Int J Appl Glass Sci.* 2012;3(1):29–35.
26. Marsh DM. Plastic flow in glass. *Proc R Soc London Ser A Math Phys Sci.* 1964;279(1378):420–35.
27. Kermouche G, Barthel E, Vandembroucq D, Dubujet P. Mechanical modelling of indentation-induced densification in amorphous silica. *Acta Mater.* 2008;56(13):3222–8.
28. Gadelrab KR, Bonilla FA, Chiesa M. Densification modeling of fused silica under nanoindentation. *J Non-Cryst Solids.* 2012;358(2):392–8.
29. Keryvin V, Meng J-X, Gicquel S, Guin J-P, Charleux L, Sanglebœuf J-C, et al. Constitutive modeling of the densification process in silica glass under hydrostatic compression. *Acta Mater.* 2014;62:250–7.
30. Molnár G, Ganster P, Tanguy A, Barthel E, Kermouche G. Densification dependent yield criteria for sodium silicate glasses—An atomistic simulation approach. *Acta Mater.* 2016;111:129–37.
31. Molnár G, Kermouche G, Barthel E. Plastic response of amorphous silicates, from atomistic simulations to experiments—a general constitutive relation. *Mech Mater.* 2017;114:1–8.
32. Mantis B, Kermouche G, Barthel E, Tanguy A. Impact of pressure on plastic yield in amorphous solids with open structure. *Phys Rev E.* 2016;93(3):033001.
33. Perriot A, Barthel E, Kermouche G, Quérel G, Vandembroucq D. On the plastic deformation of soda-lime glass—a Cr³⁺ luminescence study of densification. *Philos Mag.* 2011;91(7–9):1245–55.
34. Bruns S, Johanns KE, Rehman HUR, Pharr GM, Durst K. Constitutive modeling of indentation cracking in fused silica. *J Am Ceram Soc.* 2017;100(5):1928–40.
35. Oliver WC, Pharr GM. An improved technique for determining hardness and elastic-modulus using load and displacement sensing indentation experiments. *J Mater Res.* 1992;7(6):1564–83.
36. Winterstein-Beckmann A, Möncke D, Palles D, Kamitsos EI, Wondraczek L. A Raman-spectroscopic study of indentation-induced structural changes in technical alkali-borosilicate glasses with varying silicate network connectivity. *J Non-Cryst Solids.* 2014;405:196–206.
37. Neuville DR, de Ligny D, Henderson GS. Advances in Raman spectroscopy applied to earth and material sciences. In: Henderson GS, Neuville DR, Downs RT, editors. *Spectroscopic methods in mineralogy and materials sciences. Reviews in Mineralogy & Geochemistry*, 78. Chantilly: Mineralogical Soc Amer & Geochemical Soc, 2014; p. 509–41.
38. Winterstein-Beckmann A, Möncke D, Palles D, Kamitsos EI, Wondraczek L. Raman spectroscopic study of structural changes induced by micro-indentation in low alkali borosilicate glasses. *J Non-Cryst Solids.* 2014;401:110–4.
39. Salter PS, Baum M, Alexeev I, Schmidt M, Booth MJ. Exploring the depth range for three-dimensional laser machining with aberration correction. *Opt Express.* 2014;22(15):17644–56.
40. Benzine O, Bruns S, Pan Z, Durst K, Wondraczek L. Local deformation of glasses is mediated by rigidity fluctuation on nanometer scale. *Adv Sci (Weinh).* 2018;5(10):1800916.
41. Mound BA, Pharr GM. Nanoindentation of fused quartz at loads near the cracking threshold. *Exp Mech.* 2019;59(3):369–80.
42. Wiederhorn SM. Influence of water vapor on crack propagation in soda-lime glass. *J Am Ceram Soc.* 1967;50(8):407–14.
43. Bechgaard TK, Mauro JC, Smedskjaer MM. Time and humidity dependence of indentation cracking in aluminosilicate glasses. *J Non-Cryst Solids.* 2018;491:64–70.
44. Pallares G, Lechenault F, George M, Bouchaud E, Rountree CL, Ciccotti M. Roughness of silica glass sub-critical fracture surfaces. In: Varner JR, Wightman M, editors. *Fractography of Glasses and Ceramics VI.* 2012; p. 77–84.
45. Abaqus 2016 Online Documentation. Dassault Systèmes; 2015.
46. Han LH, Elliott JA, Bentham AC, Mills A, Amidon GE, Hancock BC. A modified Drucker-Prager Cap model for die compaction simulation of pharmaceutical powders. *Int J Solids Struct.* 2008;45(10):3088–106.
47. Kermouche G, Guillonnet G, Michler J, Teisseire J, Barthel E. Perfectly plastic flow in silica glass. *Acta Mater.* 2016;114:146–53.
48. Johnson KL. Correlation of indentation experiments. *J Mech Phys Solids.* 1970;18(2):115.
49. Jang J-I, Pharr GM. Influence of indenter angle on cracking in Si and Ge during nanoindentation. *Acta Mater.* 2008;56(16):4458–69.
50. Bruns S, Petho L, Minnert C, Michler J, Durst K. Fracture toughness determination of fused silica by cube corner indentation cracking and pillar splitting. *Mater Des.* 2020;186:108311.
51. Hill R. *The mathematical theory of plasticity.* Oxford University Press, 1998.
52. Tabor D. Indentation hardness and its measurement: some cautionary comments. In: Blau P, Lawn B, editors. *STP889-EB*

Microindentation Techniques in Materials Science and Engineering, West Conshohocken, PA: ASTM International, 1985; p. 129–59. <https://doi.org/10.1520/STP32955S>.

53. Gao XL, Jing XN, Subhash G. Two new expanding cavity models for indentation deformations of elastic strain-hardening materials. *Int J Solids Struct.* 2006;43(7–8):2193–208.
54. Narasimhan R. Analysis of indentation of pressure sensitive plastic solids using the expanding cavity model. *Mech Mater.* 2004;36(7): 633–45.
55. Ponader CW, Schroeder JF, Streltsov AM. Origin of the refractive-index increase in laser-written waveguides in glasses. *J Appl Phys.* 2008;103(6):063516.

SUPPORTING INFORMATION

Additional supporting information may be found online in the Supporting Information section.

How to cite this article: Bruns S, Uesbeck T, Fuhrmann S, et al. Indentation densification of fused silica assessed by raman spectroscopy and constitutive finite element analysis. *J Am Ceram Soc.* 2020;103:3076–3088. <https://doi.org/10.1111/jace.17024>